ACKNOWLEDGMENT

This work was performed in the context of the TARGET—"Top Amplifier Research Groups in a European Team" network and supported by IST Program of EU under contract IST-1-507893-NoE, www.target-org.net and TUBiTAK grant EEEAG 105E178.

REFERENCES

1. N. Tanzi, J. Dykstra, K. Hutchinson, A 1-Watt doubly balanced 5 GHz flip-chip SiGe power amplifier, In 2003 IEEE Radio Frequency Integrated Circuits (RFIC) Symposium, June 8–10, 2003, pp. 141–144.
2. P. Keerti, SiGe Power Devices for 802.11a wireless LAN applications at 5GHz, Electron Lett 39 (2003), 1218–1220.
3. W. Bakalski et al., A fully integrated 5.3-GHz 2.4-V 0.3-W SiGe bipolar power amplifier with 50 ohm output, IEEE J Solid State Circu 39 (2004), 1006–1014.
4. M. Maiore et al., A 63% PAE and 10:1 VSWR at 3.3 V power amplifier in 0.25/spl mu/m SiGe BiCMOS for DCS and PCS applications, In 2006 IEEE Radio and Wireless Symposium, January 17–19, 2006, pp. 247–250.
5. B.-K. Kim et al., Monolithic planar RF inductor and waveguide structures on silicon with performance comparable to those in GaAs MMIC, Proceedings of the International Electron Devices Meeting, December 10–13, 1995, pp. 717–720.
6. A. I. Khalil and P. Katzin, A low power high performance 4 GHz SiGe HBT VCO, In 2004 IEEE Microwave Theory and Techniques Symposium Digest, Fort Worth, TX pp. 1505–1508.
7. M. Falah and E. Linton, High data rate pulse regeneration using nonlinear transmission line technology (NLTL), Proceedings of the IEEE 6th High Frequency Postgraduate Student Colloquium, September 9–10, 2001, pp. 136–141.
8. E. Efshari and A. Hajimiri, A Non-linear transmission lines for pulse shaping in silicon, Proceedings of the IEEE Custom Integrated Circuits Conference, September 21–24, 2003, pp. 91–94.
9. S. Yilmaz and I. Tekin, An N-bit digitally variable ultra wide band pulse generator for GPR and UWB applications, Microwave Opt Tech Lett 48 (2006), 1334–1339, July 2006

A SYNTHETIC APERTURE RADAR-BASED FOCUSING ALGORITHM FOR B-SCAN GROUND PENETRATING RADAR IMAGERY

Enes Yigit,[1] Sevket Demirci,[1] Caner Ozdemir,[1] and Adnan Kavak[2]

[1] Department of Electrical-Electronics Engineering, Mersin University, Ciftlikkoy, Mersin 33343, Turkey; Corresponding author: cozdemir@mersin.edu.tr

[2] Department of Computer Engineering, Kocaeli University, Izmit, Kocaeli 41040, Turkey

Received 21 March 2007

ABSTRACT: *In the classical B-Scan ground penetrating radar (GPR) imagery, unprocessed image domain data exhibit undesired hyperbolic effects and therefore have low resolution features. To solve this problem, various focusing or migration techniques have been developed and applied to focus the scattered energy at their true spatial locations in the object space. In this article, we present a synthetic aperture radar (SAR) based focusing algorithm to obtain well-localized two-dimensional B-scan GPR images of various buried objects. The concept and the formulation of our frequency domain based imaging algorithm are presented. The performance of the algorithm is tested with both the simulated and measurement data. The simulation data are generated by a physical optics shooting and bouncing ray (PO-SBR) technique code; whereas the C-band measured data are collected via an experimental set-up for different ground environments. Almost perfect focusing performance is achieved for the simulated GPR images. Similarly, well-focused GPR images with high lateral resolutions are also obtained for the measurement data from metallic and non-metallic buried objects.* © 2007 Wiley Periodicals, Inc. Microwave Opt Technol Lett 49: 2534–2540, 2007; Published online in Wiley InterScience (www.interscience.wiley.com). DOI 10.1002/mop.22724

Key words: *ground penetrating radar; radar imaging; synthetic aperture radar; migration techniques*

1. INTRODUCTION

For various applications from mine detection to archeology, it is desirable to produce high resolution images of the subsurface environment from the data acquired by a ground penetrating radar (GPR) [1]. A single point scatterer shows up as a defocused, hyperbolic signature in the traditional B-scan GPR imagery due to the finite beam-width of the GPR antenna. To achieve well-resolved images of the buried objects, the GPR data collected over the surface has to be migrated from image space to object space. Several migration algorithms, aiming to focus the reflection signatures back to their true positions, have been reported in the literature [2-7]. The well-known approaches are the finite-difference migration [2], diffraction summation [3], Kirchhoff wave-equation migration [4], frequency-wavenumber ($f - k$) migration [5, 6], and reverse-time migration [7]. Most of these popular techniques are based on wave equations and have been widely used especially in seismic signal processing. The similarities between the acoustic and electromagnetic (EM) wave equations have led to the use of the same processing techniques for GPR image processing as well [6-10]. Among these, the wavenumber domain focusing techniques have been widely accepted and adapted to the modern synthetic aperture radar (SAR) imaging [11-14]. These algorithms have been developed by various groups in SAR community, and termed by different names including seismic migration [11, 12] and $f - k$ migration [13]. In the case of GPR image generation, wavenumber and space-time domain SAR-based focusing techniques are relatively new. Gunawardena [15] has applied a wave-equation based SAR method in the space-time domain. Anxue et al. [16] have used a wavenumber domain SAR migration technique to increase the resolution of the GPR image and to estimate the EM wave's velocity under the ground. More recently, Gilmore et al. [17] have compared and tested both the wavenumber domain SAR focusing technique and the seismic $f - k$ migration methods via laboratory GPR measurements. Lately, we have also developed a focusing algorithm based on hyperbolic summation (HS) technique that was successfully applied and tested with real GPR measurements [18, 19]. In this algorithm, there were some deficiencies that resulted in some unwanted defocusing effects in the resultant B-scan GPR images especially when two or more buried scatterers were close to each other.

In this work, we set out to develop and apply a frequency domain GPR focusing technique based on wavenumber SAR reconstruction algorithm to mitigate the undesired hyperbolic effects in the B-scan GPR image. The article is organized as follows: The details of the proposed method are explained in Section 2. In the next section, the algorithm is applied to a simulated data obtained by a physical optics (PO) based simulation code. The performance of the algorithm is first checked by this simulated data. Focused GPR images of various objects are presented accordingly. In Section 4, the real performance is tested by the measurement data

collected by a stepped-frequency continuous wave (SFCW) radar. Focused GPR images of several objects, buried in laboratory experimental set-up and outdoor soil environment, are provided. In the last section, the work is summarized and the issues regarding the applicability and other aspects of the algorithm are discussed.

2. SAR BASED FOCUSING ALGORITHM FOR GPR

The GPR image formation, modeled as a convolution in the spatial domain, is generally performed more efficiently in the wavenumber (k) domain. The k-domain inversion methods have the main advantage of exploiting fast Fourier transform (FFT) which provides significant computational savings. These focusing methods can be directly used in processing of GPR data when the scatterers are buried in a homogeneous medium. In [20], Soumekh proposed a $f - k$ domain SAR imaging algorithm based on the plane wave decomposition of spherical wave-fronts. In this work, we experimentally examine the near-field imaging problem of the buried objects by adapting and applying this $f - k$ domain SAR imaging algorithm to the B-scan GPR concept.

The geometrical layout of the GPR problem is shown in Figure 1(a) as the two-dimensional (2D) scattered electric field $E_s(x,f)$ is recorded for different synthetic aperture points and frequencies with the use of a SFCW radar system. As shown in Figure 1(b), the transmitted signal is composed of a number of increasing step frequencies. The radar measures the magnitude and phase of the received field for various frequencies at each spatial point. Assuming that the first starting frequency in SFCW radar is f_0 with a constant increment of Δf, the frequency of the nth sample in the received sequence is

$$f = f_0 + (n-1)\cdot\Delta f \quad n = 1,2,\cdots,M, \tag{1}$$

where M is the length of vector f. In a homogeneous environment, the frequency domain back-scattered field from the nth point scatterer at d distance from the antenna will have the form of

$$E_s(f) = \rho\cdot\exp\left(-j4\pi\frac{f}{v}d\right). \tag{2}$$

Here, ρ is the strength of the scattered electric field from the point target and v is the velocity of the EM wave in the propagation medium. For a homogeneous and lossless medium, it is obvious that $v = c/\sqrt{\varepsilon_r}$ where c is the speed of the light in free-space and ε_r is the relative electric permittivity of the medium. The signal in Eq. (2) can also be represented in terms of wavenumber as

$$E_s(f) = \rho\cdot\exp(-jk2d) \tag{3}$$

where $k = 2\pi f/v$ is the wavenumber vector of M points. This static measurement at single spatial point is nothing but an A-scan measurement [1]. In the case of our problem, the 2D B-scan data are obtained by collecting a series of A-scan measurement along a synthetic aperture axis, say x [Fig. 1(a)]. EM scatterings are summed for each discrete point as the radar antenna moves along a straight path. For a measurement point x_j on the synthetic aperture vector of N points, the distance; d from the point target at (x_0, z_0) to the sensor is equal to

$$d = \sqrt{z_0^2 + (x_j - x_0)^2} \quad j = 1,2,\cdots,N. \tag{4}$$

Before going further, we have couple of approximations in our algorithm: First, we assume that the ground medium is isotropic and homogeneous. This makes it possible to use only single velocity for the EM wave propagation. Second, we assume that the radar antenna is placed very close to air-ground surface so that the wave travels within the ground medium most of the travel time. This enables us to neglect the wave's propagation in the air medium. Under these assumptions, the B-scan received field $E_s(x,f)$ can be given as below for a total of P point targets located at different (x_i,z_i) positions.

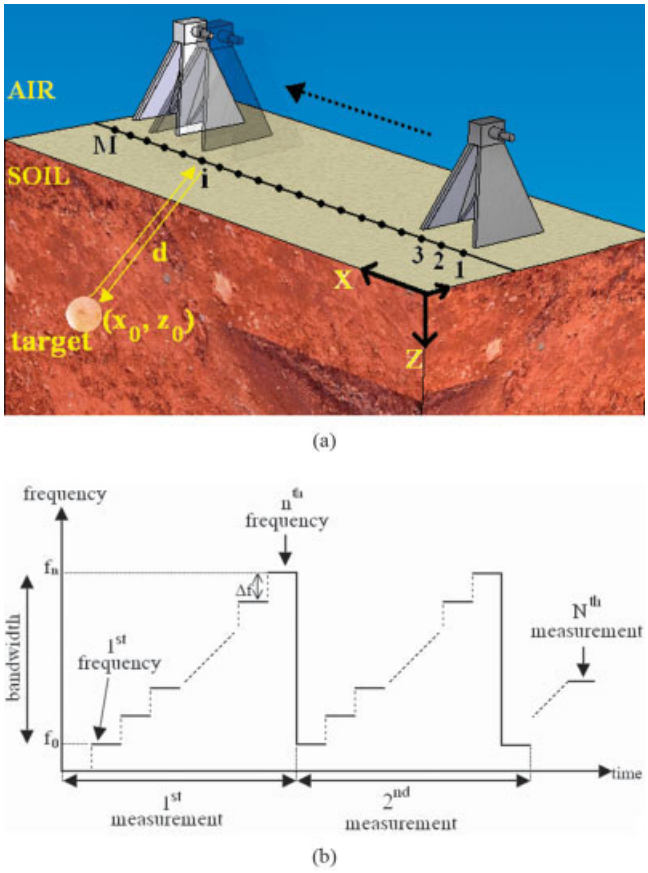

Figure 1 (a) Geometry of the monostatic B-scan GPR problem; (b) Representation of the stepped frequencies for a SFCW radar. [Color figure can be viewed in the online issue, which is available at www.interscience.wiley.com]

$$E_s(x,f) \cong \sum_{i=1}^{P}\rho_i\cdot\exp(-jk(2\sqrt{z_i^2 + (x-x_i)^2}). \tag{5}$$

Taking one-dimensional (1D) Fourier transform (FT) of Eq. (5) along the x-direction to get the field in the spatial frequency k_x domain as

$$E_s(k_x,f) = \sum_{i=1}^{P}\rho_i\cdot\int_{-\infty}^{\infty}\exp(-jk(2\sqrt{z_i^2 + (x-x_i)^2}))\cdot\exp(jk_x x)dx. \tag{6}$$

By utilizing the principle of stationary phase, above integral can be solved [21] as

$$E_s(k_x,f) = \frac{e^{-j\left(\frac{\pi}{4}\right)}}{\sqrt{4k^2 - k_x^2}} \sum_{i=1}^{P} \rho_i \cdot \exp(-jk_x \cdot x_i - j\sqrt{4k^2 - k_x^2} \cdot z_i). \tag{7}$$

Here, the ratio $e^{-j\left(\frac{\pi}{4}\right)} / \sqrt{4k^2 - k_x^2}$ is the complex amplitude term and has a constant phase. Therefore, it can be neglected for image displaying purposes. Thus, Eq. (7) can be normalized to give $\bar{E}_s(k_x,f)$ as

$$\bar{E}_s(k_x f) = \sum_{i=1}^{P} \rho_i \cdot \exp(-jk_x \cdot x_i - j\sqrt{4k^2 - k_x^2} \cdot z_i). \tag{8}$$

This is the received GPR signal data in 2D $k_x - f$ domain and has a linear phase term in x and z. However, it is obvious that a total of P point scatterers should be ideally imaged in real coordinates as in the perfect form of

$$\tilde{e}_S(x,z) = \sum_{i=1}^{P} \rho_i \cdot \delta(x - x_i, z - z_i), \tag{9}$$

where $\delta(x, z)$ is the 2D impulse function. Now, taking the 2D FT of this ideal image data with respect to x and z, we get the following scattered field value in 2D spatial-frequency domain as

$$\bar{E}_S(k_x,k_z) = \sum_{i=1}^{P} \rho_i \cdot \exp(-jk_x x_i - jk_z z_i). \tag{10}$$

The above findings claim that if we transform the received data $\bar{E}_S(k_x,f)$ to $k_x - k_z$ domain as in the form of Eq. (10), then we can get a focused-image data by simply taking 2D inverse Fourier transform (IFT) of the data in $k_x - k_z$ domain. It follows that when Eqs. (8) and (10) are compared with each other for accommodation, the transformation or spatial frequency mapping of $k_z = \sqrt{4k^2 - k_x^2}$ must be done. Applying this critical mapping, one can get the equality

$$E'_S(k_x,k_z) = E_S(k_x,f). \tag{11}$$

This implies that we must relate values of $\bar{E}_s(k_x,f)$ at each f point to the values of $E_S'(k_x,k_z)$ at k_z points with the help of the frequency mapping equation of $k_z = \sqrt{4k^2 - k_x^2}$. On the other hand, when the field data in the $k_x - f$ domain is being transferred to the $k_x - k_z$ domain, the points that are evenly spaced in the f domain will be mapped to unevenly spaced points in the k_z domain due to the nonlinear behavior of the mapping equation. To exploit the fast computation opportunity using FFT, $E_S'(k_x,k_z)$ should lie on a uniform Cartesian grid. Therefore, an interpolation procedure has to be applied in k_z domain to distribute the data into a rectangular grid in $k_x - k_z$ domain. Consequently, the final focused 2D B-scan GPR image spotting the true locations of the buried objects can be obtained by taking the 2D IFT of Eq. (11) as

$$e_S(x,z) = \frac{1}{(2\pi)^2} \int_{-\infty}^{\infty} \int_{-\infty}^{\infty} E_S'(k_x,k_z) \cdot \exp(jk_x \cdot x + jk_z \cdot z))dk_x dk_z. \tag{12}$$

If we summarize our B-scan focusing algorithm, the basic steps are listed below:

i. Collect the 2D B-scan back-scattered electric field $E_S(x,f)$ from the subsurface environment in the frequency domain
ii. Take 1D FT of $E_S(x,f)$ along synthetic aperture x to get $E_S(k_x,f)$ and normalize it to get $E_S(k_x,f)$
iii. Interpolate $E_S(k_x,f)$onto a rectangular mesh in $k_x - k_z$ domain to obtain $E_S'(k_x,k_z)$
iv. Take 2D IFT$E_S'(k_x,k_z)$ to form the final focused 2D GPR image; $e_S(x,z)$ in Cartesian coordinates.

3. SIMULATION RESULTS

The frequency-wavenumber based SAR imaging algorithm was first examined using a numerically generated B-scan GPR data obtained by using a physical optics EM scattering code that utilizes the shooting and bouncing ray (SBR) technique [22]. This simulator can effectively give the estimate of EM scattering from metallic targets in a homogeneous medium [23, 24]. Therefore, the air–soil interface was neglected during the simulation assuming that the relative permittivity of the ground medium is not too high. Considering the classical B-scan GPR set-up as in Figure 1(a), the following parameters were used during the simulation: The relative permittivity of the ground medium was chosen as 2.0. The backscattered electric field data were collected along a straight path ranging from $x = -0.25$ to 1.25 m for a total of 64 evenly spaced, discrete spatial points. As the radar antenna, a half-wavelength monopole antenna at 8 GHz was used. At each spatial point, the frequency was varied from 6.82 to 9.14 GHz such that the back-scattered field data were collected for a total of 64 discrete frequencies. Therefore, a 64-by-64 2D spatial-frequency B-scan GPR data was gathered after the EM simulation of a pipe, a mine-like cylindrical object and a plate. The computer aided design (CAD) view of these objects is shown in Figure 2(a). As seen from the figure, they were buried at different locations. The diameter and length of the pipe are 12 and 50 cm, respectively. It is put horizontally at $x = 0$ cm, $z = 30$ cm. The mine-like cylindrical object with a diameter of 30 cm and a height of 11 cm was also positioned horizontally at ($x = 50$ cm, $z = 40$ cm). The 10 cm $\times$ 10 cm metal plate was buried flat at $x = 95$ cm, $z = 30$ cm. The 2D B-scan GPR image in spatial-depth domain is obtained by taking the 1D IFT of the back-scattered signal data along the frequency domain [Fig. 2(b)]. As expected, the raw GPR image of the simulated objects exhibits the hyperbolic defocusing characteristic. It is worth noting from the image that the hyperbolic behavior for the pipe is more pronounced than the flat ones as one can expect. The outlines of the objects are drawn as lines for referencing purposes. After applying the proposed focusing method, we generated the new GPR image as shown in Figure 2(c). While applying the method, a sinc (sinus cardinalis) type interpolation scheme [25] was employed to map the data onto a uniform grid in $k_x - k_z$ domain. As seen from Figure 2(c), the resultant image is successfully focused and estimates better the location of the dominant scattering points from the buried objects when compared to the image in Figure 2(b).

4. MEASUREMENT RESULTS

4.1. Laboratory Measurements

We constructed an experimental set-up shown in Figure 3 to perform real B-scan GPR measurements in the laboratory. A large wooden pool with a size of 190 cm $\times$ 100 cm $\times$ 80 cm was constructed and filled with homogeneous and dry sand material. The relative permittivity of the sand was measured approximately

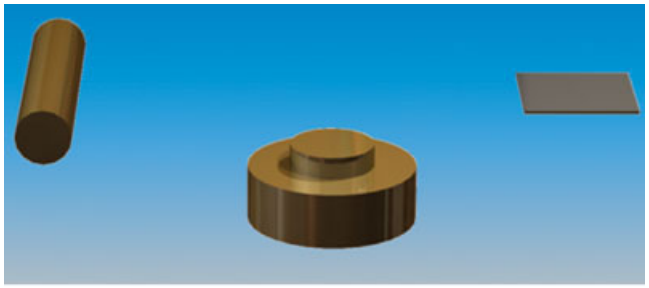

(a)

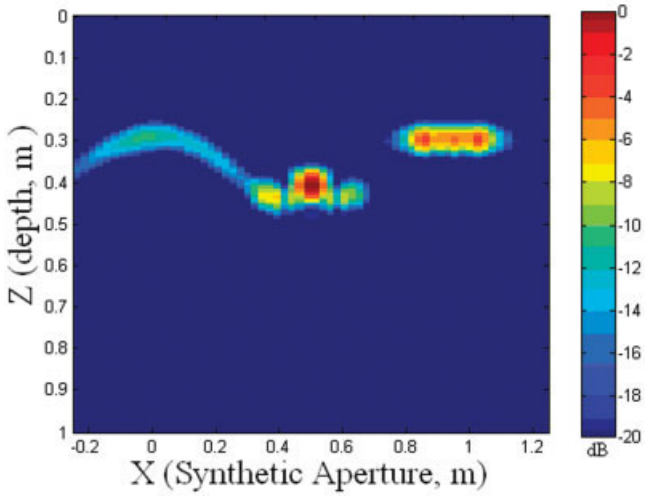

(b)

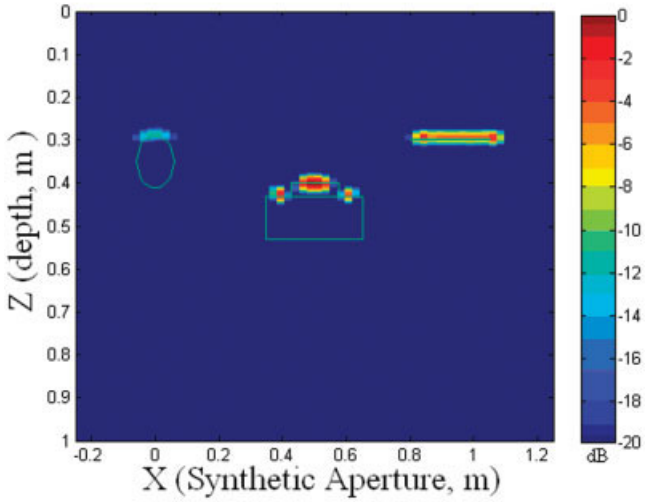

(c)

Figure 2 (a) CAD view of a pipe, a mine-like object and a plate; (b) Original defocused GPR image; (c) Focused GPR image after applying the proposed algorithm. [Color figure can be viewed in the online issue, which is available at www.interscience.wiley.com]

2.4 within the frequency band of 5.0 to 8.0 GHz. We assembled a SFCW radar using Agilent E5071B ENA vector network analyzer (VNA) and different C-band pyramidal rectangular horn antennas. The automated measurement data from the VNA was recorded to a computer via VNA's GPIB port. A typical experiment scene is pictured in Figure 4.

We have conducted a couple of B-scan GPR measurements to test the focusing performance of the algorithm. In the first experiment, two metal pipes were buried at different locations. A thin pipe with 4.5 cm in diameter and 45 cm in length was buried horizontally at $x = 35$ cm, $z = 30$ cm and a relatively thicker pipe with 6 cm in diameter and 32 cm in length was buried horizontally at $x = 75$ cm, $z = 35$ cm. The geometry of the buried objects and the sand pool is illustrated in Figure 5(a). During the experiment, sand's surface is organized to be very rough to investigate the effect of air–ground surface to the total scattered energy. Two C-band pyramidal rectangular horn antennas were put aside, positioned just above the surface and operated in bistatic mode. Forward transmission coefficient (S_{21}) measurements were collected along a straight path of 120 cm with 61 discrete spatial points. For each spatial point, the VNA's frequency was varied from 4.0 to 7.1 GHz with 15.5 MHz frequency steps to have a total of 201 discrete frequency points. The raw B-scan GPR image is acquired by taking the 1D IFT of the measured spatial-frequency

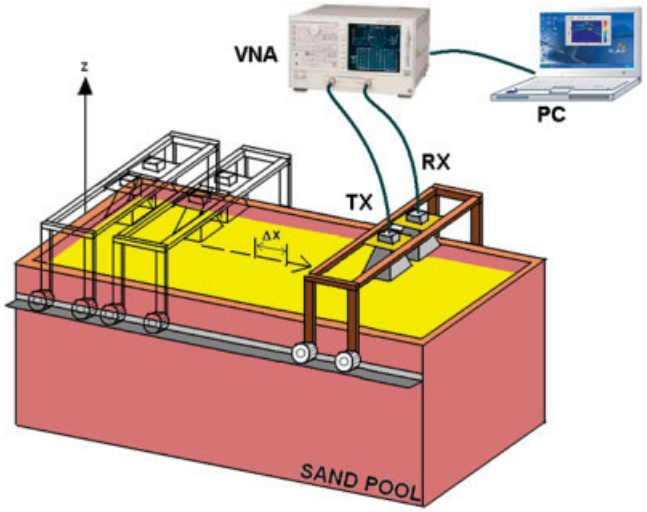

Figure 3 B-scan experimental set-up for bistatic configuration. [Color figure can be viewed in the online issue, which is available at www.interscience.wiley.com]

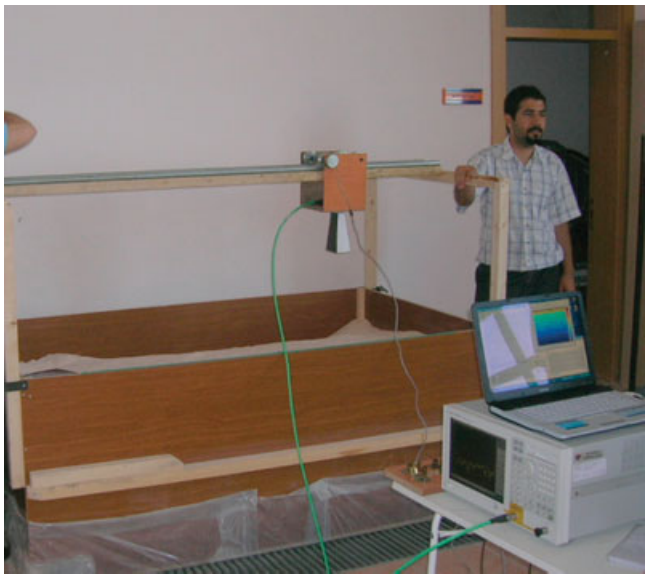

Figure 4 A scene from a laboratory measurement. [Color figure can be viewed in the online issue, which is available at www.interscience.wiley.com]

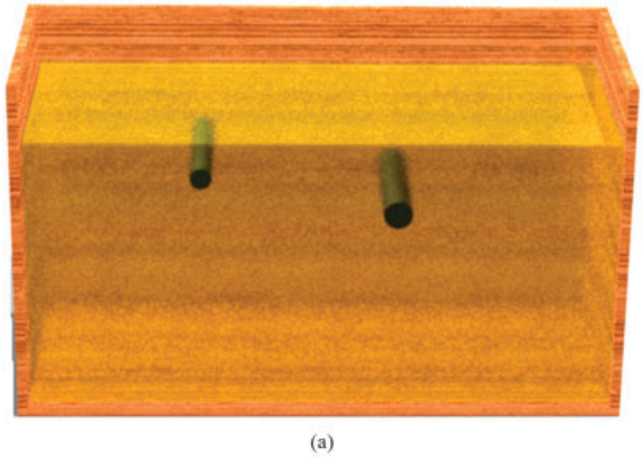

(a)

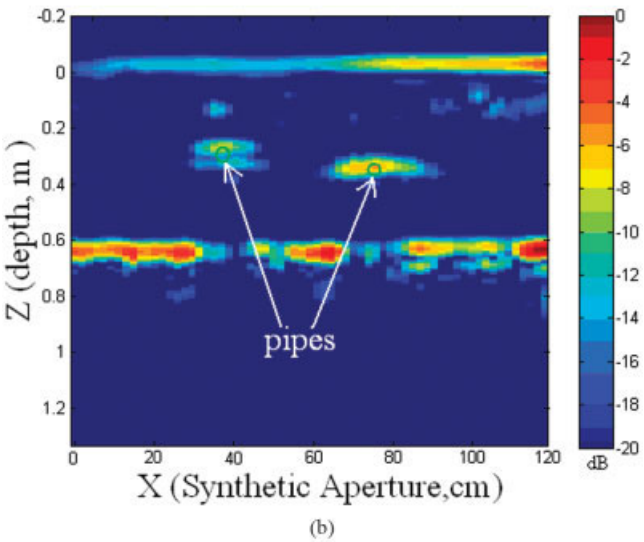

(b)

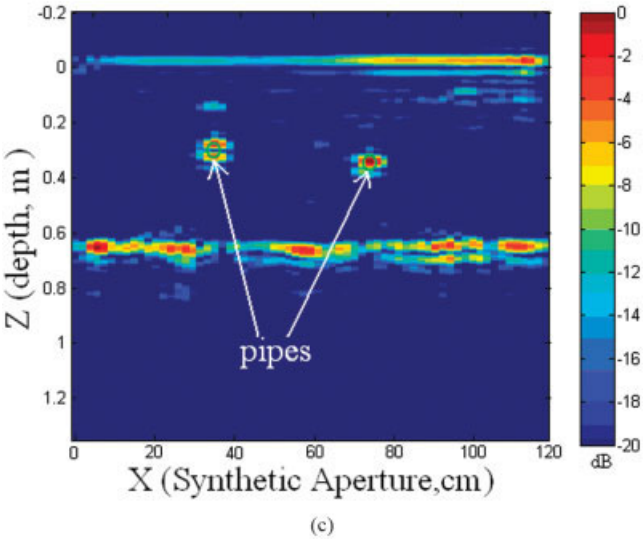

(c)

Figure 5 (a) Configuration of two metallic pipes experiment; (b) Classical GPR image (bistatic case); (c) Focused image after the proposed algorithm. [Color figure can be viewed in the online issue, which is available at www.interscience.wiley.com]

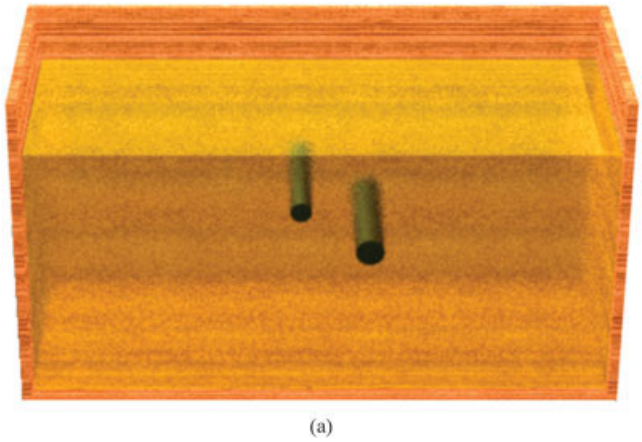

(a)

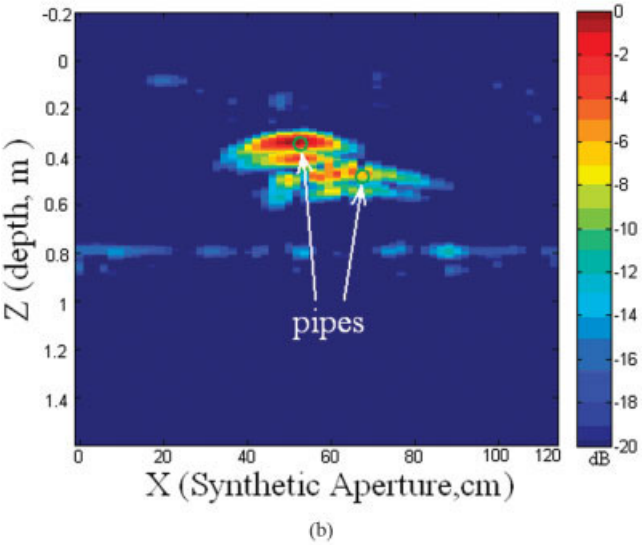

(b)

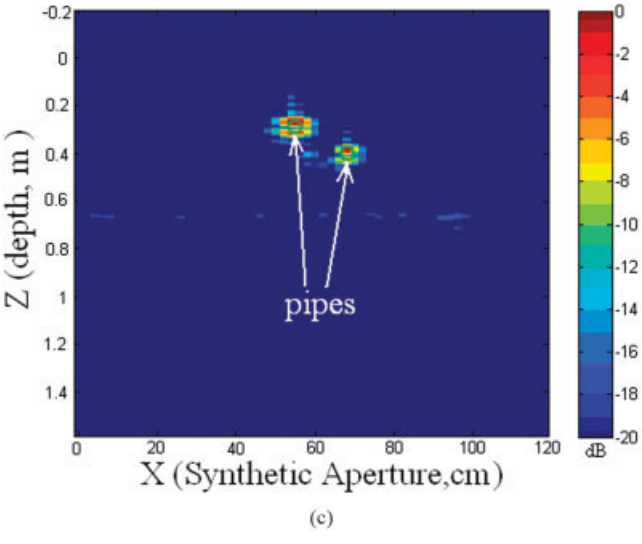

(c)

Figure 6 (a) Configuration of two closely placed pipes experiment; (b) Classical GPR image (bistatic case); (c) Focused image after the proposed algorithm. [Color figure can be viewed in the online issue, which is available at www.interscience.wiley.com]

domain data as shown in Figure 5(b). Because of the good homogeneity and low relative permittivity of the sand medium, the objects are clearly discernible in the image as hyperbolas but with low lateral resolutions. The reflections from air–ground surface and sandbox's bottom surface can also be seen with significant intensity values in the image. After applying our $f - k$ based SAR focusing algorithm, we obtained the new focused GPR image as in

Figure 7 A scene from a real soil measurement. [Color figure can be viewed in the online issue, which is available at www.interscience.wiley.com]

Figure 5(c). During inversion, again a sinc-type interpolation scheme is employed to map the data in a rectangular grid in $k_x - k_z$ domain. After applying the proposed focusing method, the scattering mechanisms have become more concentrated around the true location of the pipes. Two major scattering mechanisms are clearly visible from each pipe. The dominant scattering from the top of the pipes are very well focused. The creeping wave scatterings as the EM waves travel around the perimeter of the pipes are also focused well at the bottom of the pipes.

In the second experiment, the horizontal distance between the metal pipes was reduced to investigate the algorithm's ability in resolving close targets. For this purpose, the same thin and thicker pipes were buried flat at $x = 55$ cm, $z = 30$ cm and $x = 70$ cm, $z = 40$ cm, respectively [Fig. 6(a)]. We operated the antennas again in bistatic mode but this time we used a smooth sand surface to examine the effect of surface roughness to EM wave's penetration to the sand medium. The same frequency and spatial parameters were used as in the previous experiment. The raw GPR image obtained by taking 1D IFT of the measured spatial-frequency data as illustrated in Figure 6(b). Following observations could be easily made from this image: (i) The smoothness of sand surface affects the EM reflection from the air-ground surface as this particular scattering is highly reduced and almost invisible within the 20 dB dynamic range of the display. (ii) Since most of the transmitted energy could penetrate into the homogeneous sand medium, the scattering from the bottom surface of the pool is also clearly visible at $z = 70$ cm for the whole synthetic aperture of 120 cm. (iii) Scattering from the metal pipes experience the hyperbolic behavior as expected. The tails of these hyperbolas interact because the pipes are close to each other. (iv) Creeping wave scatterings can also be seen in the image but still demonstrating the undesired hyperbolic behavior. After applying our $f - k$ based SAR algorithm, a well-focused image is obtained as shown in Figure 6(c). The same interpolation scheme is applied as done before during mapping. The scattering mechanisms from the pipes can be clearly distinguished from each other at their true locations with good resolution in both range and cross-range directions.

4.2. *Real Soil Measurements*

We conducted a monostatic B-scan experiment with a C-band double-ridged horn antenna in outdoor soil environment to test the effectiveness of our proposed algorithm. A picture from the soil experiment is given in Figure 7. Three objects were buried flat at different locations. A bottle of water with a size of 6 cm × 6 cm × 25 cm was buried at $x = 20$ cm, $z = 15$ cm, a metal pipe with 7 cm in diameter and 33 cm in length was put at $x = 68$ cm, $z = 18$ cm and a thin metal plate with a cross section of 7 cm × 7 cm was buried at $x = 115$ cm, $z = 20$ cm,

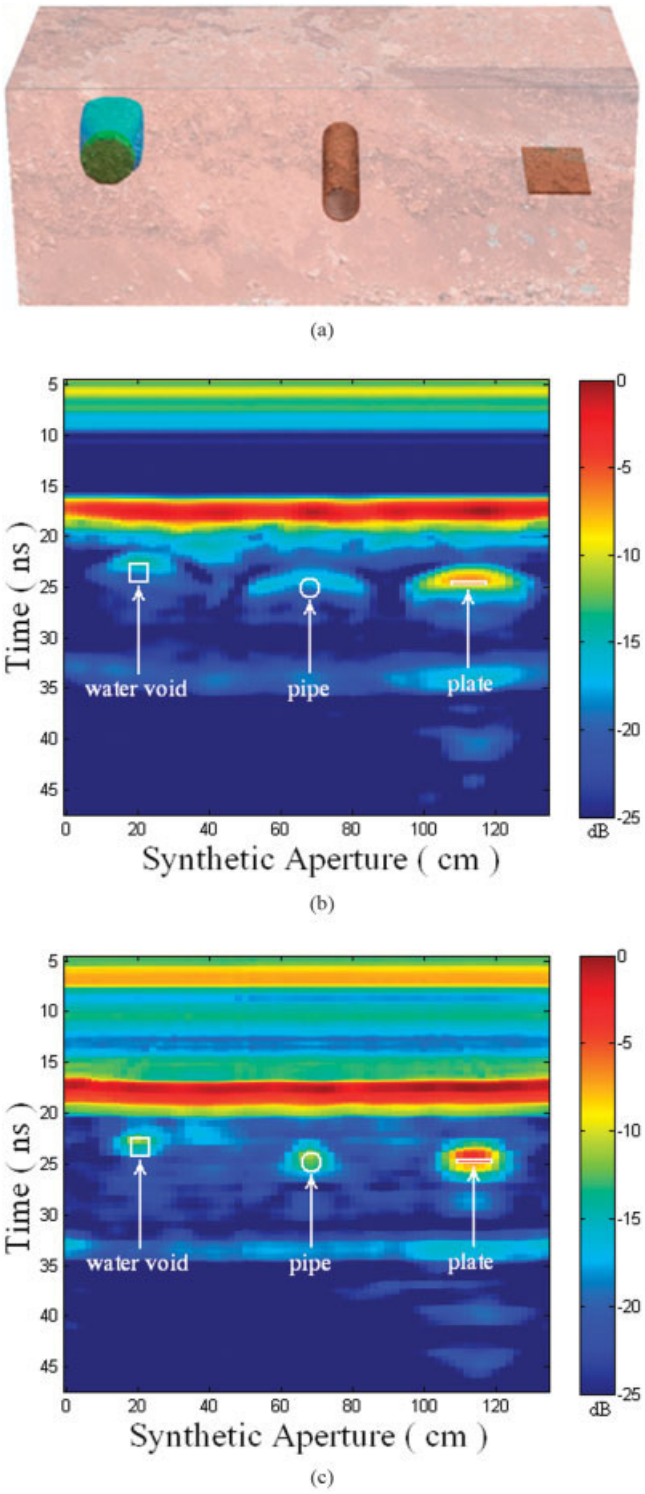

Figure 8 (a) Configuration of a bottle of water, a pipe and a plate in real soil; (b) Traditional GPR image (monostatic case); (c) Focused image after the proposed algorithm. [Color figure can be viewed in the online issue, which is available at www.interscience.wiley.com]

as illustrated in Figure 8(a). During the B-scan process, the backscattering parameter (S_{11}) measurements were taken at 2 cm spacing along a straight path of 134 cm. At each spatial point, the frequency of the VNA was stepped between 0.8 and 5 GHz with 8.4 MHz increments. Since the relative permittivity of the soil is unknown, the space-time image [Fig. 8(b)] was obtained by simply taking the 1D IFT of the spatial-frequency data along the frequency axis. The dominant scattering mechanism from air–ground surface is easily detected around at $t = 18$ ns and seen throughout the whole synthetic aperture. As expected, the unprocessed GPR image in Figure 8(b) is unfocused around the buried objects. After applying our algorithm, well focused images of the three buried objects are successfully acquired as depicted in Figure 8(c). The same interpolation technique just as in the previous cases was employed in this study as well. The dominant scattering mechanisms from buried objects are clearly identified at their true locations with resolutions in either direction.

5. CONCLUSION

In this work, we presented a frequency domain version of $f - k$ based SAR focusing technique for B-scan GPR imagery. The formulation of the algorithm was given in detail. The algorithm is first tested with a set of simulated data obtained by an EM simulation code. Almost perfect focusing was achieved after applying the proposed technique to the simulated GPR data. The performance of the method was also checked by laboratory sandpool and outdoor soil experiments. Measured B-scan GPR images of metallic and nonmetallic objects after applying the algorithm demonstrate the real performance of the method. The algorithm successfully focuses any hyperbolic behavior with good fidelity without distorting any flat behavior such as air-ground interface in the image. Thanks to sharp focusing feature of the method, resolutions in the new 2D GPR images are so good that even very close scattering mechanisms can be easily distinguished. This can be seen from Figures 5(c) and 6(c), where the scattering from the top of the pipes can be easily discerned from the creeping wave scattering mechanisms. The necessary interpolation step in the algorithm is the main source of the numerical noise in the resultant focused GPR images.

ACKNOWLEDGMENTS

This work was supported by the Scientific and Research Council of Turkey (TUBITAK) under grant no. EEEAG-104E085. The authors are grateful to Mersin Trakya Cam A.çS. for providing sand material and to Department of Mechanical Engineering of Mersin University for providing laboratory facilities for the experiments conducted.

REFERENCES

1. D. J. Daniels, Surface-penetrating radar, IEE Press, London, 1996.
2. J. F. Claerbout and S. M. Doherty, Downward continuation of move out-corrected sesimograms, Geophysics 37 (1972), 741–768.
3. D. Miller, M. Oristaglio, and G. Beylkin, A new slant on seismic imaging: Migration and integral geometry, Geophysics 52 (1987), 943–964.
4. W. A. Schneider, Integral formulation for migration in two and three dimensions, Geophysics 43 (1978), 49–76.
5. J. Gazdag, Wave equation migration with the phase-shift method, Geophysics 43 (1978), 1342–1351.
6. R. H. Stolt, Migration by Fourier transform, Geophysics 43 (1978), 23–48.
7. E. Baysal, D. D. Kosloff, and J. W. C. Sherwood, Reverse time migration, Geophysics 48 (1983), 1514–1524.
8. C. J. Leuschen and R. G. Plumb, A matched-filter-based reverse-time migration algorithm for ground-penetrating radar data, IEEE Trans Geosci Remote Sens 39 (2001), 929–936.
9. K. Gu, G. Wang, and J. Li, Migration based SAR imaging for ground penetrating radar systems, IEE Proc Radar Sonar Navigat 151 (2004), 317–325.
10. J. Song, Q. H. Liu, P. Torrione, and L. Collins, Two-dimensional and three-dimensional NUFFT migration method for landmine detection using ground-penetrating radar, IEEE Trans Geosci Remote Sens 44 (2006), 1462–1469.
11. C. Cafforio, C. Prati, and F. Rocca, Full resolution focusing of Seasat SAR images in the frequency-wave number domain, J Robot Syst 12 (1991), 491–510.
12. C. Cafforio, C. Prati, and F. Rocca, SAR data focusing using seismic migration techniques, IEEE Trans Aerospace Electron Syst 27 (1991), 194–207.
13. A. S. Milman, SAR imaging using the w-k migration, Int J Remote Sens 14 (1993), 1965–1979.
14. H. J. Callow, M. P. Hayes, and P. T. Gough, Wavenumber domain reconstruction of SAR/SAS imagery using single transmitter and multiple-receiver geometry, Electron Lett 38 (2002), 336–337.
15. A. Gunawardena and D. Longstaff, Wave equation formulation of synthetic aperture radar (SAR) algorithms in the time-space domain, IEEE Trans Geosci Remote Sens 36 (1998), 1995–1999.
16. Z. Anxue, J. Yansheng, W. Wenbing, and W. Cheng, Experimental studies on GPR velocity estimation and imaging method using migration in frequency-wavenumber domain, In: Proceedings ISAPE, Beijing, China, 15–18 August 2000, pp. 468–473.
17. C. Gilmore, I. Jeffrey, and J. LoVetri, Derivation and comparison of SAR and frequency-wavenumber migration within a common inverse scalar wave problem formulation, IEEE Trans Geosci Remote Sens 44 (2006), 1454–1461.
18. C. Ozdemir, S. Demirci, E. Yigit, and A. Kavak, A hyperbolic summation method to focus B-Scan ground penetrating radar images: An experimental study with a stepped frequency System, Microwave Opt Technol Lett 49 (2007), 671–676.
19. C. Ozdemir, S. Demirci, and E. Yigit, A focusing method for B-Scan GPR images, In: 11th International Conference on GPR, Columbus, OH, USA, 19–22 June 2006.
20. M. Soumekh, A system model and inversion for synthetic aperture radar imaging, IEEE Trans Image Process 1 (1992), 64–76.
21. W. C. Chew, Waves and fields in inhomogeneous media, 2nd ed., IEEE Press, New York, 1995.
22. H. Ling, R. Chou, and S. W. Lee, Shooting and bouncing rays: Calculation the RCS of an arbitrary shaped cavity, IEEE Trans Antennas Propagat 37 (1989), 194–205.
23. C. Ozdemir, R. Bhalla, L. C. Trintinalia, and H. Ling, ASAR—Antenna synthetic aperture radar imaging, IEEE Trans Antennas Propagat 46 (1998), 1845–1852.
24. C. Ozdemir and H. Ling, ACSAR—Antenna coupling synthetic aperture radar imaging algorithm, J Electromagn Waves Applicat 13 (1999), 285–306.
25. R. Hanssen and R. Bamler, Evaluation of interpolation kernels for SAR interferometry, IEEE Trans Geosci Remote Sens 37 (1999), 318–321.

THE CALCULATION OF DIELECTRIC DISPERSIVE MODELS IN THZ RANGE WITH GA

Wanhua Zhu, Chao Li, Guoqing Zhang, and Guangyou Fang
Institute of Electronics, Chinese Academy of Sciences(CAS), No.19, Beisihuanxi Road, Beijing, China; Corresponding author: zhuwanhua05@mails.gucas.ac.cn

Received 26 March 2007

ABSTRACT: *In this article, the dielectric dispersive models in Terahertz range are determined with the classical dielectric theory and genetic algorithm (GA). Four samples' models, glass, plywood, spruce-*